Original Research

Performance of a Fully Automatic Lesion Detection System for Breast DCE-MRI

Anna Vignati, PhD,[1]* Valentina Giannini, MS,[1,2] Massimo De Luca, PhD,[1] Lia Morra, PhD,[3] Diego Persano, MS,[3] Luca A. Carbonaro, MD,[4,5] Ilaria Bertotto, MD,[1] Laura Martincich, MD,[1] Daniele Regge, MD,[1] Alberto Bert, PhD,[3] and Francesco Sardanelli, MD[4,5]

Purpose: To describe and test a new fully automatic lesion detection system for breast DCE-MRI.

Materials and Methods: Studies were collected from two institutions adopting different DCE-MRI sequences, one with and the other one without fat-saturation. The detection pipeline consists of (i) breast segmentation, to identify breast size and location; (ii) registration, to correct for patient movements; (iii) lesion detection, to extract contrast-enhanced regions using a new normalization technique based on the contrast-uptake of mammary vessels; (iv) false positive (FP) reduction, to exclude contrast-enhanced regions other than lesions. Detection rate (number of system-detected malignant and benign lesions over the total number of lesions) and sensitivity (system-detected malignant lesions over the total number of malignant lesions) were assessed. The number of FPs was also assessed.

Results: Forty-eight studies with 12 benign and 53 malignant lesions were evaluated. Median lesion diameter was 6 mm (range, 5–15 mm) for benign and 26 mm (range, 5–75 mm) for malignant lesions. Detection rate was 58/65 (89%; 95% confidence interval [CI] 79%–95%) and sensitivity was 52/53 (98%; 95% CI 90%–99%). Mammary median FPs per breast was 4 (1st–3rd quartiles 3–7.25).

Conclusion: The system showed promising results on MR datasets obtained from different scanners producing fat-sat or non–fat-sat images with variable temporal and spatial resolution and could potentially be used for early diagnosis and staging of breast cancer to reduce reading time and to improve lesion detection. Further evaluation is needed before it may be used in clinical practice.

Key Words: computer aided detection (CAD); breast cancer; DCE-MRI; automatic detection; fat-saturation
J. Magn. Reson. Imaging 2011;34:1341–1351.
© 2011 Wiley Periodicals, Inc.

BREAST CANCER IS the second most common malignancy after lung cancer and the most common cancer in women (1,2). Dynamic contrast-enhanced magnetic resonance imaging (DCE-MRI) is a noninvasive imaging technique increasingly used in breast cancer diagnosis as an adjunct to conventional imaging techniques (3,4). DCE-MRI shows promise in detecting both invasive and ductal carcinoma in situ cancers, gives information on the biological aggressiveness of tumors and may be used to evaluate response to neoadjuvant chemotherapy (5–8).

However, DCE-MRI data analysis requires interpretation of hundreds of images and is therefore time-consuming (9). To reduce reporting time, lesions may be isolated by segmentation. This image processing procedure is preliminary to the extraction of quantitative information on lesion morphology, kinetics, and volume, and to distinguish viable from nonviable tissue (10). Most segmentation methods are manual or semi-automatic, have a degree of subjectivity, and therefore may suffer from high inter- and intra-observer variability (11–13). As it is not operator dependent, a fully automatic lesion segmentation process has the potential to reduce reading time and provide more reproducible results. Unfortunately, few studies have addressed automatic lesion detection and segmentation techniques for breast DCE-MRI (14–16). Furthermore, to our knowledge these methods have been tested only on non–fat-saturated (fat-sat) contrast-enhanced images. Because enhancing lesions may become isointense to adjacent fatty tissue after contrast material injection, fat-saturation has been introduced to enhance the contrast between lesion and surrounding tissue and to overcome the limitations due to subtraction artifacts (7). However, fat-sat sequences introduce additional challenges for lesion segmentation, such as artifacts from inhomogeneous signal saturation and a lower contrast-to-noise-ratio between enhanced lesions and surrounding parenchyma (17).

[1]Department of Radiology, IRCC - Institute for Cancer Research and Treatment, Candiolo, Italy.
[2]Department of Electronics, Politecnico of Turin, Turin, Italy.
[3]im3D SpA, Turin, Italy.
[4]Dipartimento di Scienze Medico-Chirurgiche, Università degli Studi di Milano, Milan, Italy.
[5]IRCCS Policlinico San Donato, San Donato Milanese, Milan, Italy.
Contract grant sponsor: PIIMDMT Project – Regione Piemonte, Fondo Europeo di sviluppo Regionale; Contract grant administrator: Fondazione Piemontese per la Ricerca sul Cancro (FPRC).
*Address reprint requests to: A.V., c.so E. Gamba 39 scala F, 10144 Torino, Italy. E-mail: vignati.anna@gmail.com
Received September 21, 2010; Accepted May 23, 2011.
DOI 10.1002/jmri.22680
View this article online at wileyonlinelibrary.com.

© 2011 Wiley Periodicals, Inc.

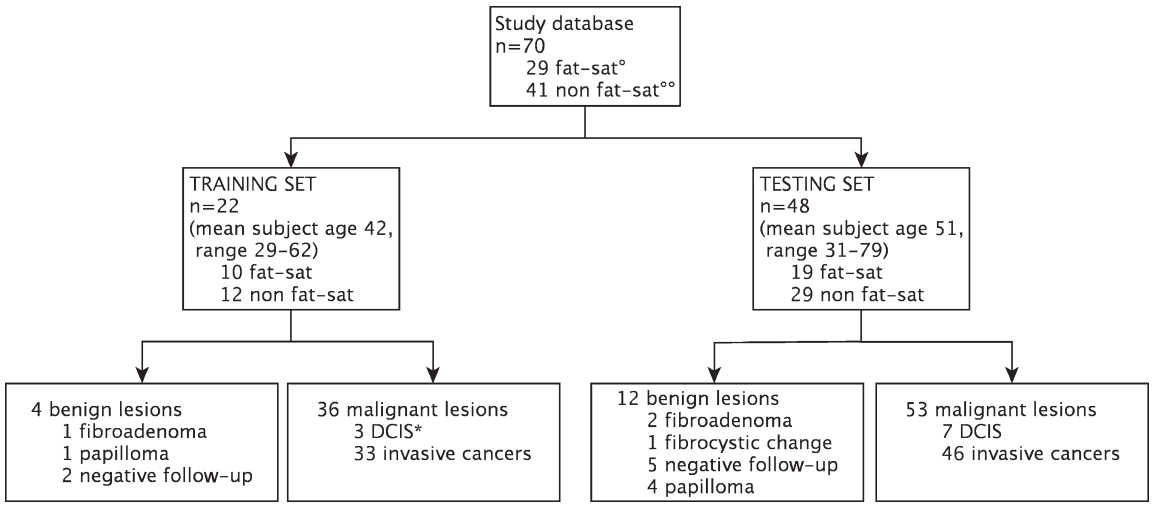

Figure 1. Flow diagram showing main demographic, clinical and technical information of the study database. °Fat-sat = fat-saturation scans. °°Non–fat-sat = non–fat-saturated images. *DCIS = Ductal Carcinoma In Situ.

The main aim of this study is to assess the per-lesion sensitivity of a new, fully automatic algorithm for breast lesion detection. The method has been developed to run on both fat-sat and non–fat-sat DCE-MRI datasets obtained from different MR scanners.

MATERIALS AND METHODS

Patient Population and Study Design

The study consisted of a validation of a new algorithm for the detection of breast lesions on DCE-MRI. Studies were collected from two institutions, each of them using a different MRI equipment and a different protocol. The Local Ethical Committee approved the retrospective use of the database for scientific purposes and waived the need for informed consent. The study was conducted in accordance with national legislation and the declaration of Helsinki.

The reference standard was surgery and histological evaluation or follow-up in some benign lesions. Enhanced areas smaller than 5 mm in diameter, the so-called *foci* according to the definition of the American College of Radiology (ACR) Breast Imaging Reporting and Data System (BI-RADS) for breast MRI, were not evaluated. In the majority of cases, these *foci* are due to a focal proliferation of glandular tissue, known as focal adenosis (7).

MRI Protocols

Group A included all studies acquired on a 1.5 Tesla (T) scanner (Signa Excite HDx, General Electric Healthcare, Milwakee, WI) using a eight-channel breast radiofrequency coil and a fat-sat three-dimensional (3D) axial fast spoiled gradient-echo sequence (VIBRANT®, General Electric) with the following technical parameters: repetition time/echo time (TR/TE) = 4.5/2.2 ms, flip angle 15°, reconstructed matrix 512 × 512, field of view 32 cm, slice thickness 2.6 mm, pixel size 0.39 mm^2. A total of seven scans were acquired for each study: one baseline, 5 contrast-enhanced frames with 50-s time resolution, and one delayed frame acquired 7 minutes after contrast injection. Gadopentetate dimeglumine (Gd-DPTA, Magnevist, Bayer-Schering, Berlin, Germany) was administered at a dose of 0.1 mmol/kg at 2 mL/s, followed by 20 mL of saline solution at the same rate.

Group B comprised studies performed on a different 1.5T scanner (Sonata Maestro Class, Siemens, Erlangen, Germany), using a dynamic 3D axial spoiled fast low angle shot sequence using a four-element two-channel coil, with the following technical parameters: TR/TE = 11/4.9 ms, flip angle 25°, matrix 512 × 512, field of view 384 mm, slice thickness 1.3 mm, pixel size 0.56 mm^2. Gd-BOPTA (MultiHance, Bracco, Milan, Italy) was used as contrast agent, administering 0.1 mmol/kg at 2 mL/s, followed by 20 mL of saline solution at the same rate. One baseline scan was acquired before contrast injection, followed by 5 contrast enhanced frames taken 118 s apart. Fat-sat sequences were not performed in group B patients.

Database Development

A training and a testing set were developed by randomly selecting studies from the 2 groups. The training set was used to optimize the parameters of the algorithms, whereas system performances were evaluated on the testing set. The characteristics of the training set are detailed in Figure 1. Lesion greatest diameter was measured manually by an experienced radiologist with an electronic caliper on the axial plane at its maximum extension. Median diameter was 16 mm (range, 12–37 mm) for benign lesions and 19 mm (range 5–90 mm) for malignant lesions; 6 of the 36 malignant lesions were sized 10 mm or less.

Image Processing

The detection pipeline (CADBREAST MRI, research version, im3D) consists of four main processing steps: breast segmentation, image registration, lesion detection and false positive (FP) reduction, none of which

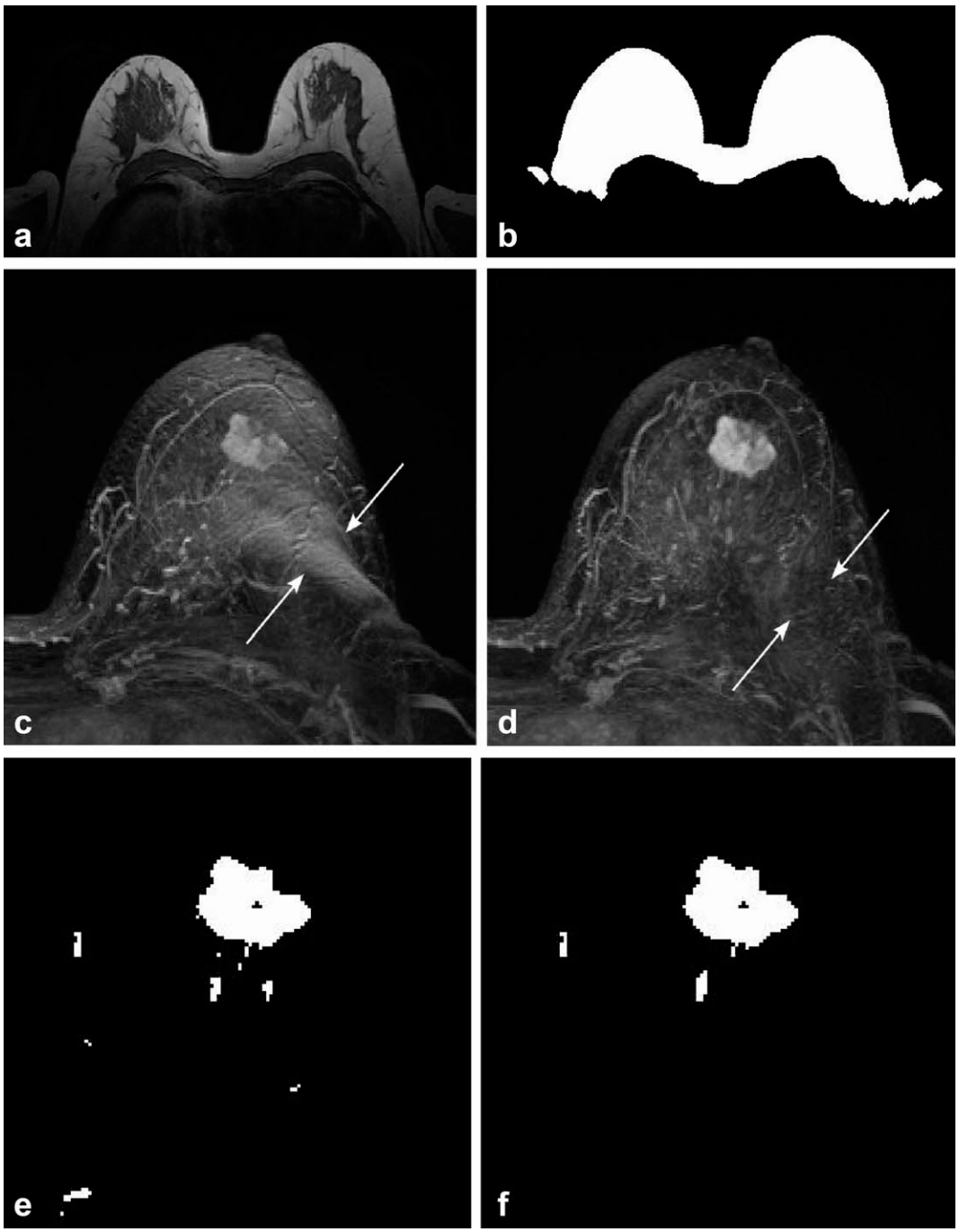

Figure 2. Main steps for breast segmentation and lesion detection for a non–fat-sat study. The unenhanced frame is shown in (**a**); the mask resulting from breast segmentation is shown in (**b**). In (**c**) the maximum intensity projection (MIP) along the z axis of the second enhanced subtracted frame is shown before registration: subtraction artifacts due to patient movement are visible as spurious enhancing voxels (arrows). In (**d**) the same subtracted MIP after registration is shown: motion artifacts have been removed (arrows). In (**e**) the results of automatic lesion detection are shown, while in (**f**) the segmentation results after false positive reduction by means of morphological and kinetic criteria are illustrated.

requires user interaction (see also Fig. 2). Breast segmentation automatically identifies the breast and axillary regions to reduce the computational burden and prevent FPs due to enhancing structures (such as the heart and extra-breast vessels). The contrast-enhanced images are then registered to the unenhanced image to correct for possible misalignments in the dynamic sequence due to patient's movement. The lesion detection step consists in the extraction of suspicious contrast enhanced areas and the FP reduction step identifies and discards regions incorrectly extracted.

Breast Segmentation

This process includes the identification of the approximate size and location of each breast, and the breast

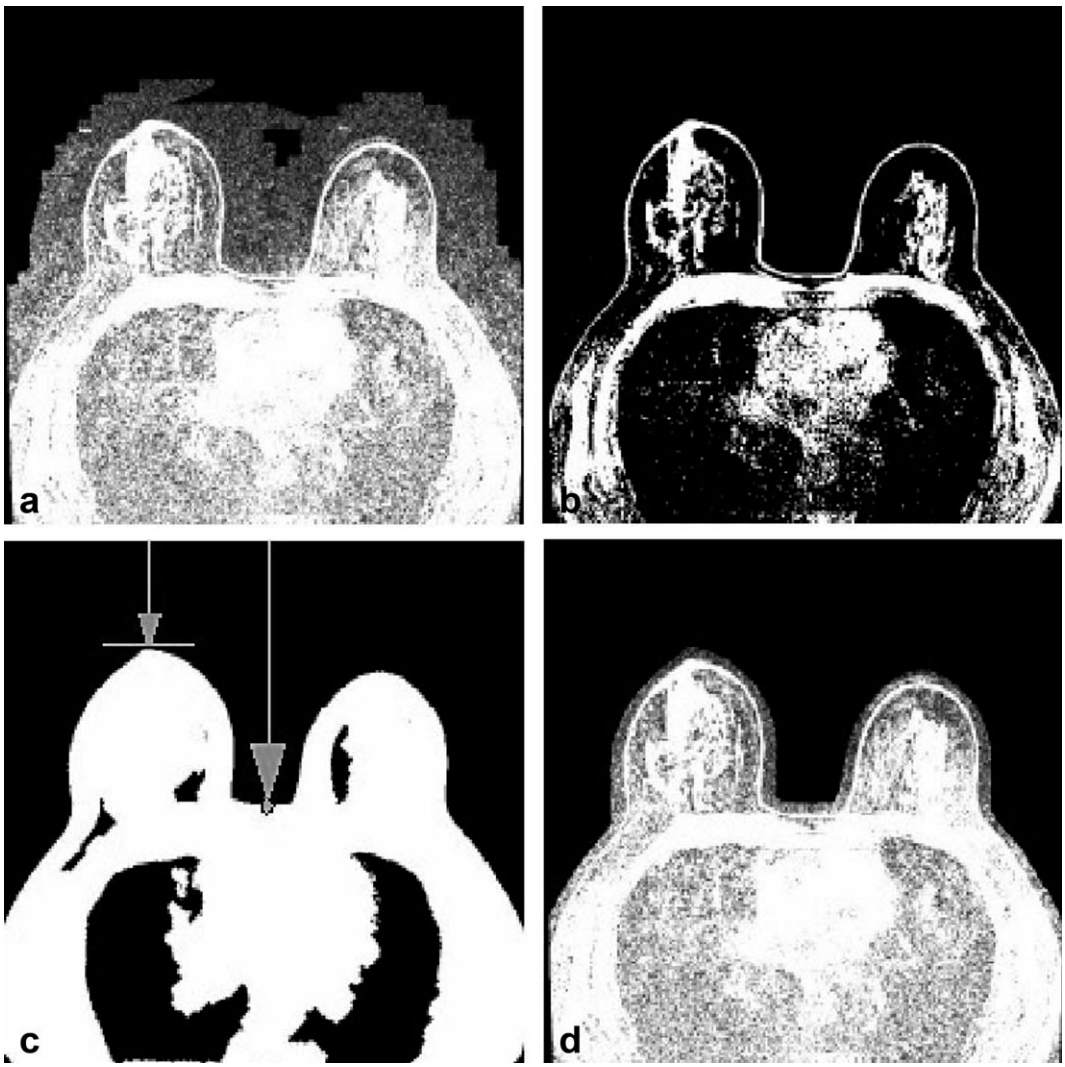

Figure 3. Procedure for identification of the breast maximum point and central line. **a**: Unenhanced image. **b**: Result of Otsu's thresholding. The largest connected region comprises also the skin profile. **c**: Result of morphological operations (6 dilations and 6 erosions, both with kernel $5 \times 5 \times 5$). For each slice, each vertical line is scanned until the patient body is reached. The position of the central line and the breast maximum point—shown by arrows—are identified. **d**: The mask obtained at step (c) is also used to remove external air from the unenhanced image to suppress noise and artifacts in the external air.

segmentation itself. A rough estimate of breast location was obtained by identifying the most anterior point reached by the breasts, which is defined as the *maximum point*, and the *minimum point* which is the deepest point within the concavity between the breasts, as shown in Figure 3. These measures were obtained following a rough segmentation of the patient's body. To separate the skin and internal structures from external air, Otsu's thresholding algorithm (18) was applied to the unenhanced images. This algorithm also allows for removing air from lungs and other low intensity areas. Because of the high intensity noise, the Otsu thresholding algorithm may generate areas in the external air. To remove these areas, the largest connected region, i.e., the breasts, was selected by the algorithm and morphological operations were then applied to fill holes (six dilations and six erosions, both using a $5 \times 5 \times 5$ kernel). The algorithm then searches for the *maximum point*, as previously defined, on the Otsu mask (Fig. 3c). The central line, defined as the line running along the concavity between the breasts, was computed by exploiting image symmetry and by searching for the skin voxel around the center of each slice (see Fig. 3).

If fat-sat is not used, the breasts can be easily identified based on the high signal intensity of fat tissue. Similarly to the technique used by Twellmann et al (16), a satisfactory segmentation can be obtained by applying morphological operations such as hole filling and dilation (6 steps with a $3 \times 3 \times 3$ kernel) to the thresholding results obtained by means of Otsu's method.

On the contrary, if fat-sat is used, intensity alone is not sufficient to obtain a reliable segmentation. Therefore, we have exploited an a priori knowledge of the main anatomical structures in the field of view using an atlas-based segmentation scheme. A simplified atlas was used in which the breasts, heart, chest wall and lungs have been manually segmented and color-coded.

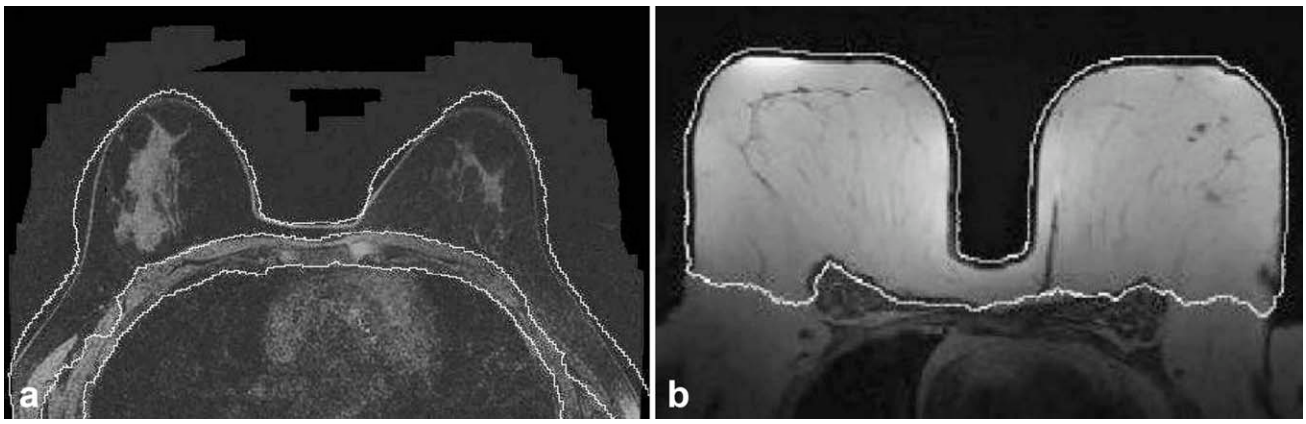

Figure 4. **a**: Example of breast segmentation for a study acquired with fat-saturation. The breast mask extends further than in non–fat-sat sequences, as defined by the breast atlas. **b**: Example of breast segmentation for a study acquired without fat-saturation.

Because breast size and shape may vary considerably across subjects, three different atlases were generated for large, medium and small breasts. The most appropriate model was automatically selected for each patient according to breast size, measured as the distance between the maximum point, and the minimum point along the central line. The large model was chosen for patients with estimated breast size larger than 10 cm, medium for patients with estimated breast size between 7 and 10 cm, and small for patients with estimated breast size smaller than 7 cm.

The patient body was identified by Otsu's thresholding method described above to mask noise present in the external air (Fig. 3). The image was then downsampled at 1.25 mm $\times$ 1.25 mm $\times$ 2.6 mm resolution to reduce the computational burden and registered to the appropriate breast atlas.

Two examples of breasts segmentation results are shown in Figure 4. The two methodologies yield slightly different results in the axillary area, but this is not compromising for the lesion detection. Axillae, supraclavicular fossae, chest wall, and anterior mediastinum can be assessed by breast MRI (e.g. to search for enlarged lymph nodes) but their evaluation could be omitted as there is no evidence of its diagnostic value (17).

Registration

This step is aimed at correcting possible misalignment in the dynamic sequence due to patient motion. It was performed by registering all the contrast-enhanced images with reference to the unenhanced sequence. Registration consists of two main steps. First, the global misalignment was compensated by using a translation and a rigid-body transformation. Subsequently, local motion was corrected by a *free-form deformation* model based on *B-splines* (19). In all cases, mutual information was used as image similarity measure, in particular by the method specified by Mattes et al (20). Optimization was carried out by means of a gradient descent optimizer for the rigid registrations, and of the LBFGSB (*Limited memory - Broyden, Fletcher, Goldfarb, and Shannon - for Bound constrained optimization*) optimizer for the nonrigid sub-step (21). Finally, the original contrast-enhanced frames were warped to obtain the transformed (aligned) contrast-enhanced frames by applying the respective deformation field. In the warping, *B-spline* interpolation was used to minimize the introduction of sampling artifacts. An example of how registration was able to compensate for motion artifacts is shown in Figure 5.

Lesion Detection

Contrast enhancement of breast lesions shows large physiologic variations, mostly depending on differences in vascular permeability (22,23) and other technical and physiological parameters, including type and dose of contrast material (24,25). Differences may depend on lesion histology, on the timing of imaging or on inhomogeneities within the lesions, such as those observed in necrotic areas or in fibrosis. To take into account for the nonuniform uptake of contrast, while reducing at the same time the computational burden associated with the processing of all the contrast-enhanced registered frames, we used the subtracted mean intensity projection image over time (mIPT). Being the dynamic sequence a 4D image ($x \times y \times z \times t$), where t is time, the mIPT is the 3D image ($x \times y \times z$) formed by averaging each voxel along the t axis. Subtraction of the unenhanced frame was performed to neglect the contribution of regions which do not show contrast enhancement.

Different scanners, coils, acquisition modalities, types and amounts of contrast agent injected, patients' physiology, and other external factors, result in significant variations of image intensities among images acquired in different hospitals, in different patients, or even among different examinations from the same patient (24,25). To compensate for these effects, the subtracted mIPT was normalized by contrast enhancement of the mammary vessels.

Because the mammary vessels show maximum contrast enhancement in the early frames of the dynamic sequence, they were automatically segmented on the first subtracted contrast-enhanced frame.

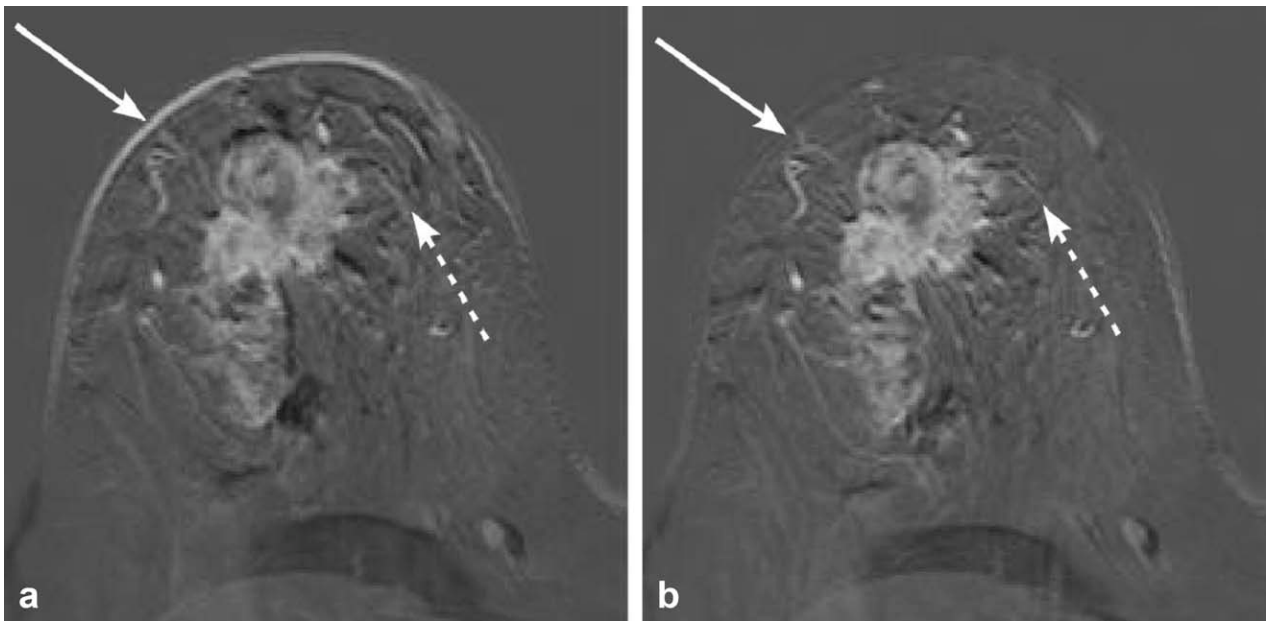

Figure 5. Comparison between subtracted images with and without registration. A slice from a non–fat-sat examination is shown. **a**: Subtraction artifacts due to patient movement are visible along the breast profile (plain arrow), in the breast parenchyma (dot arrow), at lesion and vessel borders, as well as at the borders of fat lobules. These artifacts may introduce spurious enhancing voxels, thus increasing the number of false positive findings at segmentation. **b**: Subtraction artifacts are dramatically reduced when elastic registration is used.

A suitable ROI was automatically selected based on the position of the central line by placing a rectangle of a fixed size (50 mm × 100 mm) in each slice, with the exception of the upper 30% and lower 10% of the 3D image slices that were not considered because the mammary vessels are not usually visible. The mammary vessels were then identified by applying to the ROI the multiscale 3D Sato's vessel enhancement filter, which is based on the eigenvalues of the Hessian matrix (26,27).

The Sato's vessel enhancement filter considers the mutual magnitude of the *eigenvalues* as indicative of the shape of the underlying object: isotropic structures are associated with eigenvalues which have a similar nonzero magnitude, while vessels present one negligible and two similar nonzero eigenvalues. Let the eigenvalues of the Hessian matrix be λ_1, λ_2, λ_3 (with $\lambda_1 > \lambda_2 > \lambda_3$). On a given scale, vesselness is thus defined as:

$$V_\sigma(\lambda_1;\lambda_c) = \begin{Bmatrix} \exp\left(-\frac{\lambda_1^2}{2(a_1\lambda_c)^2}\right) & if & \lambda_1 \le 0, \lambda_c \neq 0 \\ \exp\left(-\frac{\lambda_1^2}{2(a_2\lambda_c)^2}\right) & if & \lambda_1 > 0, \lambda_c \neq 0 \\ 0 & if & \lambda_c = 0 \end{Bmatrix}, \quad [1]$$

where $\lambda_c = \min(\lambda_2, \lambda_3)$, α_1 and α_2 were set to 0.5. The σ footer in $V\sigma$ indicates that the vesselness is computed on a smoothed version of the image and is therefore representative of the variations of image intensity on the σ spatial scale. As vessels in the breasts could have different diameters, the vesselness is evaluated on a range of spatial scales, and the highest response is selected for each voxel. Specifically, the vesselness response is computed at 6 exponentially distributed scales between the maximum and minimum scales $\sigma_{min} = 0.5$ and $\sigma_{max} = 1.0$.

The most vessel-like voxels were selected by applying a threshold equal to half the maximum vesselness value observed in the ROI identified as described above. Figure 6 shows an example of mammary vessels.

The normalization factor was calculated as the mean contrast enhancement of the mammary vessel voxels in the first contrast-enhanced frame. After normalizing the subtracted mean intensity projection, regions showing contrast enhancement were extracted. Even if the contrast-enhanced frames were normalized, we have found that a fixed threshold was not suitable to successfully segment lesions on all scans. A global threshold T_I was empirically determined as:

$$T_I = mean_I + \frac{\max_I}{3}, \quad [2]$$

where $mean_I$ is the mean value of the normalized intensity histogram of the breast and axillary region and max_I is the highest intensity value observed in the same region.

Because lesions are often connected to feeding vessels, they are often segmented together. To prevent lesion oversegmentation, which could reduce the diagnostic quality of the segmentation and limit the performance of segmentation-based CAD applications, voxels belonging to vessels were excluded from lesion detection. For each voxel, the *eigenvalues* of the covariance matrix were extracted, and the ratio between the highest and medium eigenvalues was used as a vesselness measure. Voxels with a ratio larger than a fixed threshold T_v (where $T_v = 10$) were labeled as vessels and excluded from lesion detection. Connected components were then extracted from the resulting mask.

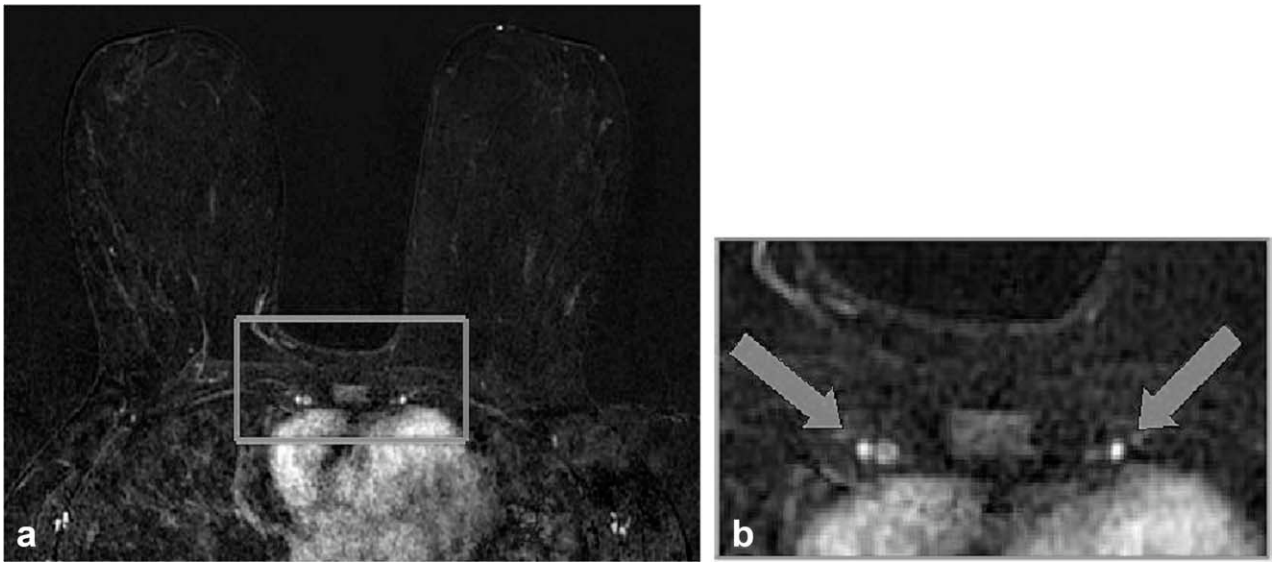

Figure 6. a: First subtracted contrast-enhanced frame with the region where the mammary vessels are located in the rectangle. **b**: Zoom of the region in the rectangle highlighted in (a). Arrows point mammary arteries that will be segmented by the system.

False Positive Reduction

The regions showing contrast enhancement include not only benign or malignant lesions, but also FPs such as motion artifacts and noise. Moreover, not all vessels are completely discarded during the lesion detection step, and hence still contribute to the number of FPs. A few heuristic criteria were applied in our algorithm to discard FPs. First, regions with a volume of less than 20 mm^3 were excluded. Taking into account image resolution and possible lesion undersegmentation, this roughly corresponded to a lesion of 5 mm in diameter, which is the cutoff between *foci* and lesions (28).

Contrast enhancement kinetics can be classified as curves I, II and III with an increasing probability of malignancy (6%, 64%, and 87%, respectively) (29). However, these curves are commonly referred to individual voxels or to a set of few contiguous voxels within a plane belonging to a single part of tissue with uniform vascular characteristics, and thus homogeneous contrast enhancement, whereas the average intensity curve calculated over an entire lesion (typically without homogeneous vascular characteristics) is generally more similar to the average signal intensity curves shown in Figure 7. Thus, our aim was to identify trends which are indicative of structures other than benign and malignant lesions, such as noise, artifacts or vessels.

Empirically, some simple kinetic features were found to identify trends rather typical of vessels or artifacts, as shown in Figure 7. For instance, artifacts due to noise and patient motion are usually characterized by high signal variations; hence, regions with standard deviation greater than 150, or with a higher-than-10% decrease or increase in signal intensity in the last frame, with respect to the second-last frame, were discarded. Furthermore, regions with mean intensity decreasing from the first to the second enhanced frame are discarded, as this pattern is found in vessels but not in lesions.

Statistical Analysis

The results of the registration and breast segmentation steps were visually inspected by a radiologist with more than 4 years of experience in breast MRI. The radiologist labeled a finding as a true positive if the lesion was confirmed at histology or at follow-up, otherwise it was defined as a FP. Detection rate was calculated as the number of true positives (both malignant and benign) over the total number of lesions as defined at the reference standard, whereas sensitivity was calculated as the number of malignant lesions detected by the system over the total number of malignant lesions. Lesions were grouped according to size as follows: from 5 to 10 mm, 11 to 20 mm, and larger than 20 mm (30) and detection rate and

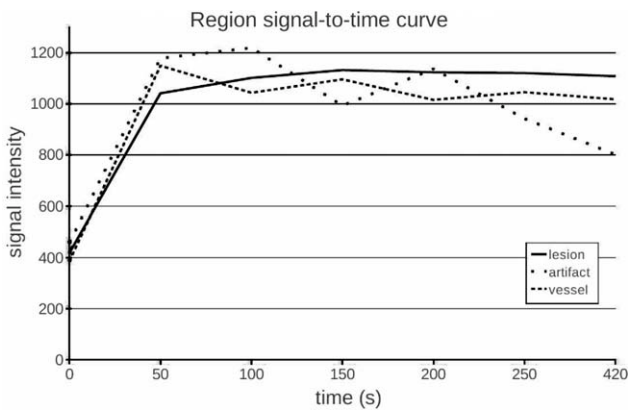

Figure 7. Signal intensity curves calculated over an entire connected component in the case of a lesion, a vessel and an artifact.

Table 1
Number of Lesions and Performance for Each Dimension Group

Lesions Dimension (mm)	# Malignant	# Benign	# Total	Detection Rate (Upper-Lower Limits; 95% CI)	Sensitivity (Upper-Lower Limits; 95% CI)
5–10	6	10	16	69% (44% – 86%)	100% (61% – 100%)
11–20	13	2	15	87% (62% – 96%)	92% (67% – 99%)
>20	34	0	34	100% (90% – 100%)	100% (90% – 100%)
Total	**53**	**12**	**65**	**89% (79% – 95%)**	**98% (90% – 99%)**

Lesions were grouped according to the National Cancer Institute. Detection rate and sensitivity were calculated with a 95% confidence interval.

sensitivity were calculated for each group. Sensitivity and detection rate values are presented with 95% confidence intervals (CIs) using the Wilson method for single proportions. Detection rate and sensitivity were also separately calculated for fat-sat and non–fat-sat exams, and the χ^2 test was used to assess differences between the two subgroups. The detection rate of the system for lesions satellite to index cancers detected by radiologists for which a lesion-by-lesion pathological analysis was not reported, was analyzed separately.

FP findings were defined by the radiologist as mammary or extra-mammary findings, and characterized either as vessels, image artifacts (i.e., skin, chemical shift, patient movements, etc), lymph nodes, normal gland or other findings (i.e., nipple, pectoral muscle, heart, etc). The FP median, 1st and 3rd quartiles were calculated for the entire testing set, for the fat-sat and non–fat-sat subgroups. A two-sided Kruskal Wallis test was applied to test for differences between the medians for the total number of FP/patient.

A P level lower than 0.05 was considered statistically significant.

RESULTS

Algorithm performance was evaluated on a dataset of 48 DCE-MRI studies performed on women with suspicion of breast cancer based on conventional imaging. Relevant demographic, clinical and technical information on the dataset is shown in the flow chart in Figure 1. The median of the largest diameter of benign and malignant lesions was, respectively, 6 mm (range, 5–15 mm) and 26 mm (range, 5–75 mm). Overall, there were 16 lesions sized 10 mm or less, 15 lesions between 11 and 20 mm, and 34 lesions sized larger than 20 mm.

The automatic algorithm detected 58 of the 65 lesions (89% detection rate; 95% CI 79–95%), including 52 of the 53 malignant lesions (98% sensitivity; 95% CI 90–99%). Detection rate and sensitivity according to lesion size are shown in Table 1.

In the fat-sat subgroup, 20 of the 25 lesions (80% detection rate; 95% CI 61–91%) were detected, including 19 of the 20 malignant lesions (95% sensitivity; 95% CI 76–99%). In the non–fat-sat subgroup, 38 of the 40 lesions (95% detection rate; 95% CI 84–99%) were detected, including all 33 malignant lesions (100% sensitivity; 95% CI 90–100%). Differences in sensitivity and detection rate between the two groups were not statistically significant ($P = 0.798$ and $P = 0.137$ respectively).

A total of 7 lesions with an average size of 7 ± 3 mm (mean ± SD) were missed by the algorithm, including 6 benign and 1 malignant nodules. Five of the undetected lesions were in dataset A including: 2 fibroadenomas, 2 small enhancements with a negative MRI follow-up of 5 and a 7 mm in size, respectively, and a 12-mm invasive ductal carcinoma. Missed lesions in dataset B were two 5 mm small enhancements unchanged at MRI follow-up. Examples of lesions detected and missed by the system are shown in Figure 8.

In addition to malignant lesions histologically confirmed as a result of a lesion-by-lesion analysis in the pathological report, 17 lesions satellite to malignant index lesions, with a median diameter of 7 mm (range, 5–20 mm) were detected by two radiologists. Sixteen of them (94%) were detected by the system.

Median mammary FPs per breast were 4 (1st–3rd quartiles 3–7.25), while median extra-mammary FPs per study were 2 (1st–3rd quartiles 1–5). Table 2 shows the distribution of findings according to the type. For the fat-sat subgroup, median mammary FPs per breast were 4 (1st–3rd quartiles 2–7.25); median extra-mammary FPs per study were also 4 (1st–3rd quartiles 3–6). In the non–fat-sat group, median mammary FPs per breast were 4.5 (1st–3rd quartiles 3.5–7), while median extra-mammary FPs per study were 1 (1st–3rd quartiles 1–2). No statistical significant differences were detected between the two subgroups ($P = 0.72$).

Average execution time was 5m48s for the non–fat-sat group and 8m48s for the fat-sat group. Execution time was measured on a computer equipped with a CPU Intel Core i7 940 Quad Core @#2.93GHz architecture and 8 GBytes RAM.

DISCUSSION

This study demonstrated that the fully automatic algorithm we developed for the detection of breast lesions in DCE-MRI has a high performance and is versatile as it can be used with different equipment and acquisition modes. The system achieved a sensitivity of 98%, with an acceptable number of FP findings. Moreover, the good performances obtained in detecting satellite lesions (16 of 17 were identified) highlights the system's potential in helping the detection of multifocal and multicentric breast cancers.

Fully automatic lesion detection has the potential of reducing inter- and intra-observer variability and reading time (11,13). However, few methods have

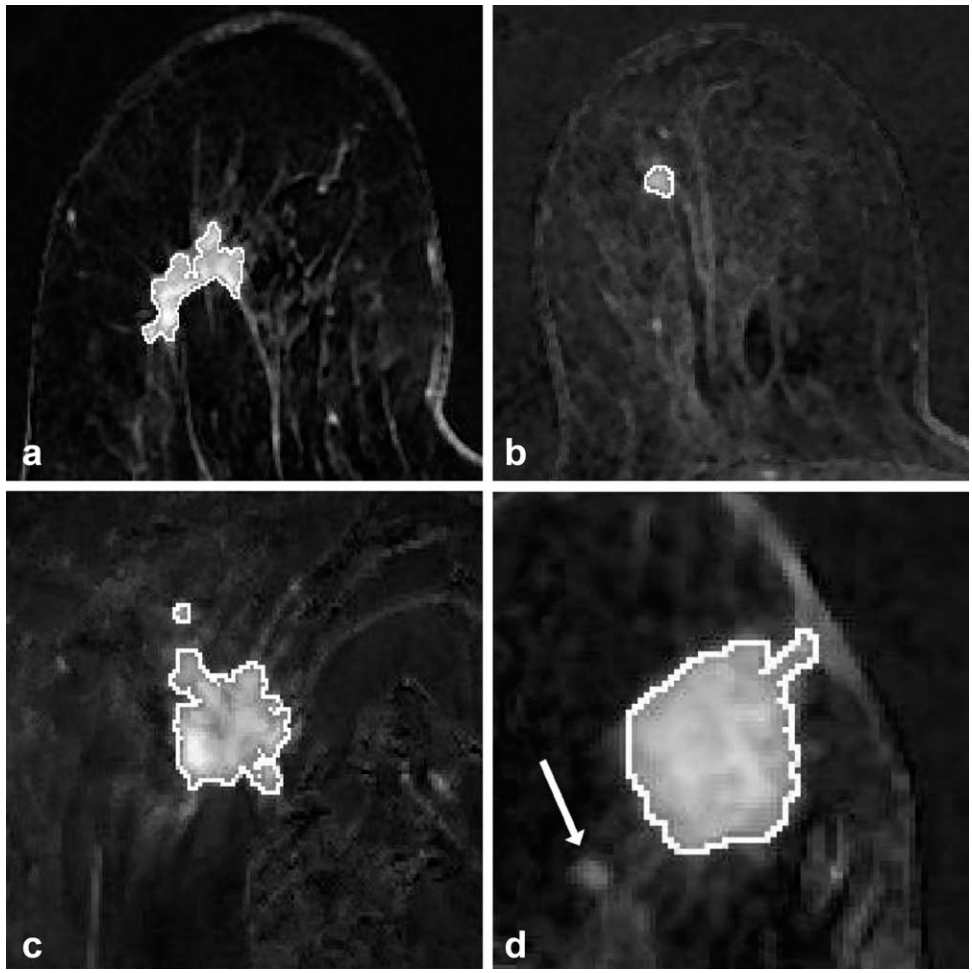

Figure 8. Examples of segmentation results, superimposed on the normalized and subtracted mean projection over time. **a**: A 33-mm invasive ductal carcinoma (fat-sat image) correctly segmented; (**b**) a 7-mm invasive ductal carcinoma (fat-sat image) correctly segmented; (**c**) a 26-mm invasive ductal carcinoma (non–fat-sat image) correctly segmented; (**d**) a 25-mm invasive ductal carcinoma (fat-sat image) correctly segmented; here a 5-mm satellite lesion (arrow) was missed by the system.

been developed to date to detect breast lesions automatically with DCE-MRI. Ertas et al developed an automatic algorithm for the detection of breast lesions based on cellular neural network segmentation and 3D template matching (14). They assessed the performance of their system on a dataset of 39 lesions, of which 19 were benign and 20 malignant. All MRI studies were performed with non–fat-sat sequences and they obtained a detection rate of 100% with less than one FP per study. An automatic lesion detection method based on support vector machine, proposed by Twellmann et al also showed promising results, yielding an area under the ROC curve of 0.98. However, the algorithm was tested on a limited dataset of 12 patients and only on non–fat-sat images (16). The above mentioned methods cannot be applied to fat-sat images as normalization is performed by dividing each enhanced images by the unenhanced one. This process yields very noisy images if fat-sat is applied, as most of the breast signal is suppressed in the unenhanced frame. Moreover, Ertas et al applied a fixed threshold to extract suspicious areas and this may limit the applicability to studies acquired with different protocols.

Our algorithm takes advantage of the following two innovative approaches. First, the normalization technique we proposed is based on the contrast enhancement of mammary vessels. Compared with normalization with respect to the unenhanced image, our approach gives stable results in the case of fat-sat images, as the obtained normalization factor is related to contrast agent administration. However, this method requires that DCE-MRI is performed on the axial plane, as the mammary vessels should be included in the field of view with an adequate spatial resolution. Second, we adopted the mIPT instead of the commonly used MIPT (maximum intensity projection over time), because it is less sensitive to noise and it produces more reliable segmentation.

There are some limitations to our method. First, the detection was obtained using the mIPT and this process could underestimate lesion size, as late enhancing voxels and voxels with a rapid washout can be

Table 2
Classification of FP findings according to the type

FP findings		
Type	#	%
vessels	267	54
artifacts*	113	23
gland	80	16
lymph nodes	2	0,4
other**	32	6

*i.e. chemical shift, skin, patient movements.
**i.e. nipple, pectoral muscle.

attenuated when averaging over time. For applications such as malignancy discrimination, a more accurate identification of lesion boundary and morphology could be useful, and a further refinement of the lesion segmentation may become necessary. However, using the MIPT also has limitations. It affects the number of FPs negatively, as it is very sensitive to artifacts and noise, and may lead to overestimation of lesion size due to the "blooming sign" effect (31–33). Second, our system has a higher number of FP findings if compared with other academic software and to commercially available solutions (34). Most of our FPs are vessels, mainly tortuous vessels or bifurcations with low vesselness values. Detection of bifurcations is a known topological problem for vessel identification and tracking (35,36). Reduction of the number of FPs can conceivably be obtained by introducing a classification stage dedicated to the recognition of vessels, and more specifically of bifurcations. Improving the accuracy of breast segmentation may also help reduce the number of FP findings. FP reduction is achieved by a set of simple heuristics criteria based on knowledge of the morphological and kinetics properties of FPs. A more efficient classifier could improve the system's FP rate. Finally, although the performances of our method are promising, we must point out that the objective of this study was solely lesion detection. Discrimination between malignant and benign lesions should be tackled in a future study, adding to our pipeline a classification step using morphological and kinetic features. All lesions included in this dataset were mass-like enhancements, but the performance on non–mass-like enhancements should be likewise evaluated.

In conclusion, in this study we presented a new, fully automatic lesion detection system for breast DCE-MRI. The method was tested on MR datasets obtained from different scanners, with a variable temporal and spatial resolution and on both fat-sat and non–fat-sat images, and has shown a high detection rate and sensitivity, balanced by a reasonable low number of FP findings. This type of system could potentially be used for early diagnosis and staging of breast cancer to reduce reading time and to improve detection, especially of the smaller satellite nodules. Further refinements are ongoing to improve vessel detection, breast segmentation, and implement lesion characterization.

REFERENCES

1. Mahoney MC, Bevers T, Linos E, Willett WC. Opportunities and strategies for breast cancer prevention through risk reduction. CA Cancer J Clin 2008;58:347–371.
2. Boyle P, Ferlay J. Cancer incidence and mortality in Europe, 2004. Ann Oncol 2005;16:481–488.
3. Sardanelli F, Giuseppetti GM, Canavese G, et al. Indications for breast magnetic resonance imaging. Consensus document "Attualita in senologia", Florence 2007. Radiol Med 2008;113:1085–1095.
4. Sardanelli F, Boetes C, Borisch B, et al. Magnetic resonance imaging of the breast: recommendations from the EUSOMA working group. Eur J Cancer 2010;46:1296–1316.
5. Chakraborti K, Bahl P, Sahoo M, Ganguly S, Oberoi C. Magnetic resonance imaging of breast masses: comparison with mammography. Indian J Radiol Imaging 2005;15:381–387.
6. Montemurro F, Martincich L, Sarotto I, et al. Relationship between DCE-MRI morphological and functional features and histopathological characteristics of breast cancer. Eur Radiol 2007;17:1490–1497.
7. Kuhl C. The current status of breast MR imaging. Part I. Choice of technique, image interpretation, diagnostic accuracy, and transfer to clinical practice. Radiology 2007;244:356–378.
8. Kuhl CK. Current status of breast MR imaging. Part 2. Clinical applications. Radiology 2007;244:672–691.
9. Fausto A, Magaldi A, Babaei Paskeh B, Menicagli L, Lupo EN, Sardanelli F. MR imaging and proton spectroscopy of the breast: how to select the images useful to convey the diagnostic message. Radiol Med 2007;112:1060–1068.
10. Bankman I, Nizialek T, Simon I, Gatewood O, Weinberg I, Brody W. Algorithms for segmenting small-low contrast objects in images. In: Suri JS, Rangayyan RM,Society of Photo-optical Instrumentation Engineers, editors. Recent advances in breast imaging, mammography, and computer-aided diagnosis of breast cancer. Bellingham, WA: SPIE Press; 2006. p 723–738.
11. Mussurakis S, Buckley DL, Horsman A. Dynamic MRI of invasive breast cancer: assessment of three region-of-interest analysis methods. J Comput Assist Tomogr 1997;21:431–438.
12. Liney GP, Gibbs P, Hayes C, Leach MO, Turnbull LW. Dynamic contrast-enhanced MRI in the differentiation of breast tumors: user-defined versus semi-automated region-of-interest analysis. J Magn Reson Imaging 1999;10:945–949.
13. Niemeyer T, Wood C, Stegbauer K, Smith J. Comparison of automatic time curve selection methods for breast MR CAD. In: Proceedings of the Medical Imaging Conference of SPIE. Volume 5370. San Diego, CA: International Society for Optical Engineering; 2004. p 785–790.
14. Ertas G, Gulcur HO, Osman O, Ucan ON, Tunaci M, Dursun M. Breast MR segmentation and lesion detection with cellular neural networks and 3D template matching. Comput Biol Med 2008;38: 116–126.
15. Woods BJ, Clymer BD, Kurc T, et al. Malignant-lesion segmentation using 4D co-occurrence texture analysis applied to dynamic contrast-enhanced magnetic resonance breast image data. J Magn Reson Imaging 2007;25:495–501.
16. Twellmann T, Saalbach A, Muller C, Nattkemper TW, Wismuller A. Detection of suspicious lesions in dynamic contrast enhanced MRI data. Conf Proc IEEE Eng Med Biol Soc 2004;1:454–457.
17. Mann RM, Kuhl CK, Kinkel K, Boetes C. Breast MRI: guidelines from the European Society of Breast Imaging. Eur Radiol 2008; 18:1307–1318.
18. Otsu N. A threshold selection method from gray-level histograms. IEEE Trans Syst Man Cybern B Cybern 1979;9:62–66.
19. Rueckert D, Sonoda LI, Hayes C, Hill DL, Leach MO, Hawkes DJ. Nonrigid registration using free-form deformations: application to breast MR images. IEEE Trans Med Imaging 1999;18:712–721.
20. Mattes D, Haynor D, Vesselle H, Lewellyn TWE. Nonrigid multimodality image registration. In: Proceedings of the Medical Imaging Conference of SPIE. Volume 4322. San Diego, CA: International Society for Optical Engineering; 2004. p 1609–1620.
21. Broyden C. The convergence of a class of double-rank minimization algorithms 1. General considerations. IMA J Appl Math 1970;6:76–90.
22. Gribbestad I, Gjesdal K, Nilsen G, Lundgren S, Hjelstuen M, Jackson A. An introduction to dynamic contrast-enhanced MRI in oncology. In: Jackson A, Buckley D, Parker GJM, editors. Dynamic contrast-enhanced magnetic resonance imaging in oncology. Heidelberg: Springer Verlag; 2005. p 3–20.
23. Heywang-Kobrunner SH, Beck R. Contrast-enhanced MRI of the breast. New York: Springer; 1996.229 p.
24. Carbonaro LA, Verardi N, Di Leo G, Sardanelli F. Handling a high relaxivity contrast material for dynamic breast MR imaging using higher thresholds for the initial enhancement. Invest Radiol 2010;45:114–120.
25. Sardanelli F, Fausto A, Esseridou A, Di Leo G, Kirchin MA. Gadobenate dimeglumine as a contrast agent for dynamic breast magnetic resonance imaging: effect of higher initial enhancement thresholds on diagnostic performance. Invest Radiol 2008;43:236–242.
26. Antiga L. Generalizing vesselness with respect to dimensionality and shape. The Insight Journal - 2007 July - December. Available at: http://hdl.handle.net/1926/576. Accessed September 10, 2010.
27. Sato Y, Nakajima S, Shiraga N, et al. Three-dimensional multi-scale line filter for segmentation and visualization of curvilinear structures in medical images. Med Image Anal 1998;2:143–168.

28. ACR Practice guideline for the performance of contrast-enhanced magnetic resonance imaging (MRI) of the breast. 2008. Available at: http://www.acr.org/secondarymainmenucategories/quality_safety/guidelines/breast/mri_breast.aspx. Accessed September 10, 2010.
29. Kuhl CK, Mielcareck P, Klaschik S, et al. Dynamic breast MR imaging: are signal intensity time course data useful for differential diagnosis of enhancing lesions? Radiology 1999;211:101–110.
30. Greene FL. American Joint Committee on Cancer, American Cancer Society. AJCC cancer staging manual, 6th edition. New York: Springer-Verlag; 2002. xiv, 421 p.
31. Dietzel M, Baltzer PA, Vag T, et al. Differential diagnosis of breast lesions 5 mm or less: is there a role for magnetic resonance imaging? J Comput Assist Tomogr 2010;34:456–464.
32. Penn A, Thompson S, Brem R, et al. Morphologic blooming in breast MRI as a characterization of margin for discriminating benign from malignant lesions. Acad Radiol 2006;13:1344–1354.
33. Fischer DR, Wurdinger S, Boettcher J, Malich A, Kaiser WA. Further signs in the evaluation of magnetic resonance mammography: a retrospective study. Invest Radiol 2005;40:430–435.
34. Kurz KD, Steirthaus D, Klar V, et al. Assessment of three different software systems in the evaluation of dynamic MRI of the breast. Eur J Radiol 2009;69:300–307.
35. Kirbas C, Quek F. A review of vessel extraction techniques and algorithms. ACM Comput Surv 2004;36:81–121.
36. Freiman M, Joskowicz L, Sosna J. A variational method for vessels segmentation: algorithm and application to liver vessels visualization. In: Proceedings of the Medical Imaging Conference of SPIE. Volume 7261. Orlando, FL: International Society for Optical Engineering; 2009. p 72610H–72618H.